THE JOURNAL OF PHYSICAL CHEMISTRY LETTERS
A JOURNAL OF THE AMERICAN CHEMICAL SOCIETY

pubs.acs.org/JPCL

Letter

Tuning the Iron−Oxygen Bond Length in α-Fe_2O_3 for Efficient Electrochemical Sensing

Cunyuan Gao,[⊥] Yutong Wang,[⊥] Na Zhang, Weiyi Wang, Qasim Imtiaz, Zhaoyong Guan,* and Bin Cai*

Cite This: *J. Phys. Chem. Lett.* 2026, 17, 5037−5044

Read Online

ACCESS | Metrics & More | Article Recommendations | Supporting Information

ABSTRACT: Transition-metal oxides are widely used as sensing interfaces, yet the lack of reliable descriptors limits the rational design of high-performance electrochemical sensors. Here we establish a direct correlation among the Fe−O bond length, adsorption energy, and electrochemical sensing activity by combining density functional theory with experimental validation. We show that shortening the Fe−O bond enhances Fe−O covalency, weakens Pb^{2+} adsorption, and improves sensitivity, thereby identifying the Fe−O bond length as a reliable activity descriptor. Guided by this principle, α-Fe_2O_3 with the shortest Fe−O bond length was optimized to yield a miniaturized electrochemical sensor with high sensitivity (26.3 μA μM^{-1}) and an ultralow detection limit (1.14 nM). The sensor enables on-site Pb^{2+} detection in real water and food samples with a performance consistent with ICP-MS analysis. These findings introduce the Fe−O bond length as a generalizable descriptor for oxide-based sensing interfaces and provide a framework for the rational design of advanced electrochemical sensing platforms.

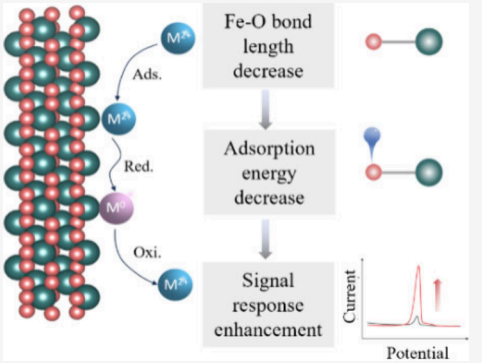

Downloaded via SHANDONG UNIV on April 30, 2026 at 09:13:41 (UTC).
See https://pubs.acs.org/sharingguidelines for options on how to legitimately share published articles.

Heavy metal contamination, especially Pb^{2+}, poses severe risks to environmental and food safety.[1,2] Industrial emissions containing Pb^{2+} ions, including wastewater and exhaust gases, can contaminate environmental media, such as soil and bodies of water. These pollutants are subsequently absorbed by crops through irrigation, undergo bioaccumulation, and eventually enter the human body via the food chain.[3] Furthermore, the use of Pb^{2+}-containing industrial additives, such as chrome yellow ($PbCrO_4$), in food processing may lead to direct migration of Pb^{2+} ions into food products,[4] posing a significant and immediate ingestion risk. Excessive Pb^{2+} exposure can induce severe neurotoxic effects, resulting in particularly serious and often irreversible damage to neurological development in children.[5,6] In response, regulatory agencies worldwide have established stringent standards to limit Pb^{2+} exposure. For instance, the World Health Organization mandates a lead concentration in drinking water not exceeding 0.01 mg L^{-1}. Similarly, the European Union enforces a lead migration limit of <0.1 mg kg^{-1} for food contact materials, while the Chinese national standard sets a maximum lead limit of 0.2 mg kg^{-1} in vegetables and related products. Therefore, the development of reliable and highly sensitive sensors for the on-site detection of Pb^{2+} in water and food is of critical importance. However, conventional analytical techniques for heavy metal ion (HMI) detection, such as atomic absorption spectrometry, inductively coupled plasma mass spectrometry, and atomic fluorescence spectrometry, rely on expensive instrumentation and involve complex operational procedures,[7−9] making the on-site detection of Pb^{2+} ions difficult.

The electrochemical detection method has advantages of simple instrumentation and easy operation, which makes it possible to detect Pb^{2+} on-site.[10−12] However, the microscopic interaction mechanism between its sensitive interface and metal ions remains unclear. This technique operates by adsorbing and reducing target HMIs at active sites on the electrochemical interface, followed by oxidative stripping at anodic potentials.[13] The electronic structure of the active site is closely related to the binding strength of HMIs, which critically determines the detection performance.[14,15] Therefore, a thorough investigation of the structure−activity relationship governing the adsorption energy of HMIs on the interface is essential for enhancing the sensing performance. Over the past few decades, transition-metal oxides have played an important role in the design of high-performance sensing interfaces for HMI detection.[5,12,16−18] Consequently, extensive efforts have been dedicated to optimizing the electronic structure of transition-metal oxides through strategies such as doping engineering,[19,20] defect engineering,[21,22] and crystal facet control.[5,23] Although these material-focused studies have significantly enhanced the sensing performance, research into the underlying mechanisms, particularly the parameters

Received: January 15, 2026
Revised: April 9, 2026
Accepted: April 10, 2026
Published: April 16, 2026

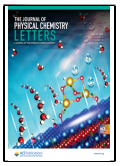

ACS Publications

© 2026 American Chemical Society

governing the sensing activity, remains limited. The establishment of convenient and reliable activity descriptors is essential to accelerate the development of novel sensing catalysts for on-site, real-time detection of Pb^{2+}.

In this study, we first employed density functional theory (DFT) calculations to evaluate the adsorption energy of Pb^{2+} on α-Fe_2O_3 surfaces with varying Fe−O bond lengths. The results showed that the adsorption energy decreases as the Fe−O bond length shortens. Guided by this insight, we experimentally tuned the Fe−O bond length by adjusting the calcination temperature and investigated its influence on the intrinsic electrochemical activity of α-Fe_2O_3 for Pb^{2+} detection. Among them, Fe_2O_3-700, which possessed the shortest Fe−O bond length, exhibited the highest sensing performance, suggesting that the Fe−O bond length can serve as a reliable and convenient activity descriptor for the electrochemical detection of HMIs. We further enhanced the surface area of Fe_2O_3-700 via ball milling, thereby increasing the number of exposed adsorption sites. The resulting miniaturized electrochemical sensor demonstrated outstanding performance, with a sensitivity of 26.3 $\mu A \cdot \mu M^{-1}$ and a detection limit of as low as 1.14 nM, and it was successfully applied for on-site detection in real water environments and food.

DFT Calculation. Electrochemical sensing of HMIs is a surface-driven process involving metal ion adsorption, electron transfer, and desorption at the sensing interface (Figure 1a,b).[15] The coordination environment of active sites critically influences the metal ion adsorption energy, thereby affecting the electrochemical signal. To elucidate this relationship, we employed DFT calculations to investigate the effect of varying Fe−O bond lengths on the adsorption energy of Pb^{2+}. Previous studies have reported four distinct magnetic configurations for α-Fe_2O_3.[24] Based on our DFT calculations, antiferromagnetic order is the most stable, which was selected as the bulk model. The symmetric distribution of the density of states (DOS) with respect to the spin-up and spin-down channels confirms the successful construction of the antiferromagnetic model (Figure S1). To isolate the influence of Fe−O bond length on Pb adsorption, we constructed a series of simplified α-Fe_2O_3 slab models by proportionally scaling the lattice constants while keeping the fractional atomic coordinates fixed. The resulting models with different Fe−O distances are shown in Figure 1c. These scaled structures were used to probe the trend in adsorption behavior as a function of Fe−O bond length rather than to reproduce the fully relaxed structures of the experimentally calcined samples.

To shed light on how the Fe−O bond length influences the desorption behavior of HMIs during electrochemical sensing, we performed DFT calculations to analyze the adsorption energies of Pb on α-Fe_2O_3 surfaces with varying Fe−O bond lengths (Figure S2). Due to the surface atomic arrangement of α-Fe_2O_3, multiple potential adsorption sites are available for *Pb. Based on DFT calculations, *Pb adsorption at the hollow site yields is the most favorable and was therefore selected for subsequent analysis. Figure 1d and Table S1 summarize the calculated adsorption energies of Pb on α-Fe_2O_3 surfaces with varying Fe−O bond lengths. As the Fe−O bond length decreases, the adsorption of Pb becomes weaker (i.e., E_{ads} becomes less negative). This trend suggests that shortening the Fe−O bond weakens Pb binding at the surface. The covalency of the Fe−O bond may provide an intrinsic explanation for this result.[25] Due to Fe−O covalent interactions, the negative charge of O^{2-} is partially transferred to Fe^{3+}, and this charge

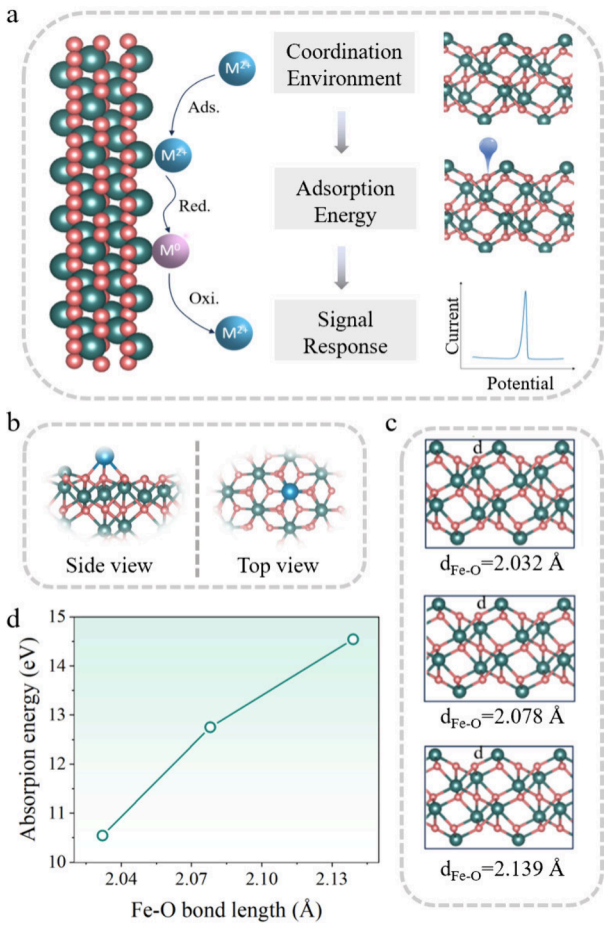

Figure 1. DFT calculations. (a) Schematic diagram of the adsorption, electron transfer, and desorption processes and influencing factors during electrochemical sensing. The coordination environment of active sites at the sensitive interface of an electrochemical sensor dictates the adsorption energy of heavy metal ions, thereby modulating the resulting electrochemical signal. (b) Side and top views of the α-Fe_2O_3 structure models after the adsorption of *Pb species. Color scheme: Fe, green; O, red; and Pb, blue. (c) Slab models for α-Fe_2O_3 of different Fe−O bond lengths. (d) Adsorption energy of *Pb on α-Fe_2O_3 with different Fe−O bond lengths.

transfer is enhanced at shorter Fe−O bond lengths. According to coordination theory, when O^{2-} carries a less negative charge, its ability to coordinate with Pb^{2+} diminishes.

Structural and Physicochemical Properties. A series of Fe_2O_3 oxides with varying Fe−O bond lengths was synthesized using a conventional sol−gel method, with the calcination temperature systematically varied (i.e., 500, 600, and 700 °C denoted as Fe_2O_3-500, Fe_2O_3-600, and Fe_2O_3-700, respectively). Figure 2a shows the powder X-ray diffraction (XRD) patterns, confirming the successful synthesis of hematite α-Fe_2O_3 (JCPDS no. 03-0664) across the calcination temperature range. Specifically, the main diffraction peaks at approximately 24.14, 33.15, 35.61, 40.85, 49.48, and 54.09° are indexed to the 012, 104, 110, 113, 024, and 116 planes of the hematite structure. Notably, no discernible peaks associated with impurities were observed, highlighting the excellent structural stability of the α-Fe_2O_3 oxides at calcination temperatures from 500 to 700 °C. As the calcination temperature increases, particle aggregation occurs, leading to a reduction in specific surface area. This trend is confirmed by Brunauer−Emmett−Teller (BET) analysis, as shown in Figure 2b and Figure S3.

https://doi.org/10.1021/acs.jpclett.6c00146
J. Phys. Chem. Lett. 2026, 17, 5037−5044

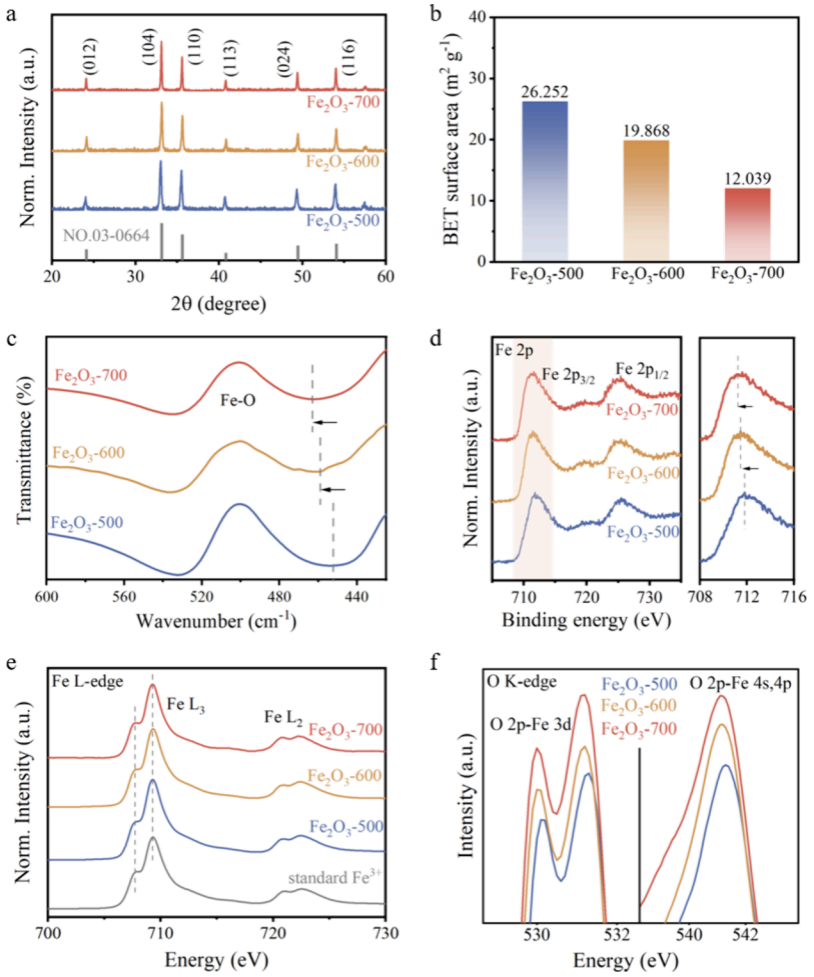

Figure 2. Structural characterization. (a) XRD patterns of the α-Fe_2O_3 oxides. (b) BET surface areas of the α-Fe_2O_3 oxides. (c) FTIR spectra of the α-Fe_2O_3 oxides. (d) XPS spectra of Fe 2p of the α-Fe_2O_3 oxides. (e) Fe $L_{2,3}$-edge XAS spectra of the α-Fe_2O_3 oxides and standard Fe^{3+}. (f) O K-edge XAS spectra of the α-Fe_2O_3 oxides.

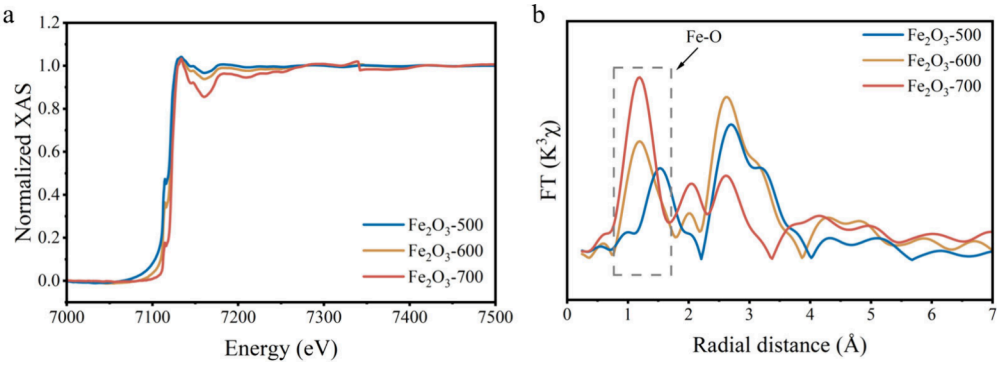

Figure 3. Fe−O bond length characterization. (a) Experimental Fe K-edge XAS spectra of the α-Fe_2O_3 oxides. (b) Experimental Fe K-edge FT-EXAFS spectra of the α-Fe_2O_3 oxides.

Specifically, the specific surface area decreases from 26.252 $m^2 \cdot g^{-1}$ for Fe_2O_3-500 to 12.039 $m^2 \cdot g^{-1}$ for Fe_2O_3-700. Fourier transform infrared (FTIR) spectroscopy was employed to probe changes in local chemical bonding (Figure 2c). The spectral band near 449 cm^{-1} corresponds to the Fe−O bond vibration.[26] As the calcination temperature increases, this peak gradually shifts to higher wavenumbers. Specifically, for Fe_2O_3-500, Fe_2O_3-600, and Fe_2O_3-700, the peaks are 453, 460, and 463 cm^{-1}, respectively. According to FTIR principles, such a blue shift indicates an increase in the vibrational frequency, which is typically associated with a shortened Fe−O bond length. The results indicate that the Fe−O bond length increases with decreasing calcination temperature, yielding the following order: Fe_2O_3-700 < Fe_2O_3-600 < Fe_2O_3-500. Figure 2d compares the Fe 2p XPS spectra of α-Fe_2O_3 oxides calcined at different temperatures. As the calcination temperature increases, the Fe $2p_{3/2}$ peak shows a slight shift toward lower binding energies, indicating a change in the electronic structure

https://doi.org/10.1021/acs.jpclett.6c00146
J. Phys. Chem. Lett. 2026, 17, 5037−5044

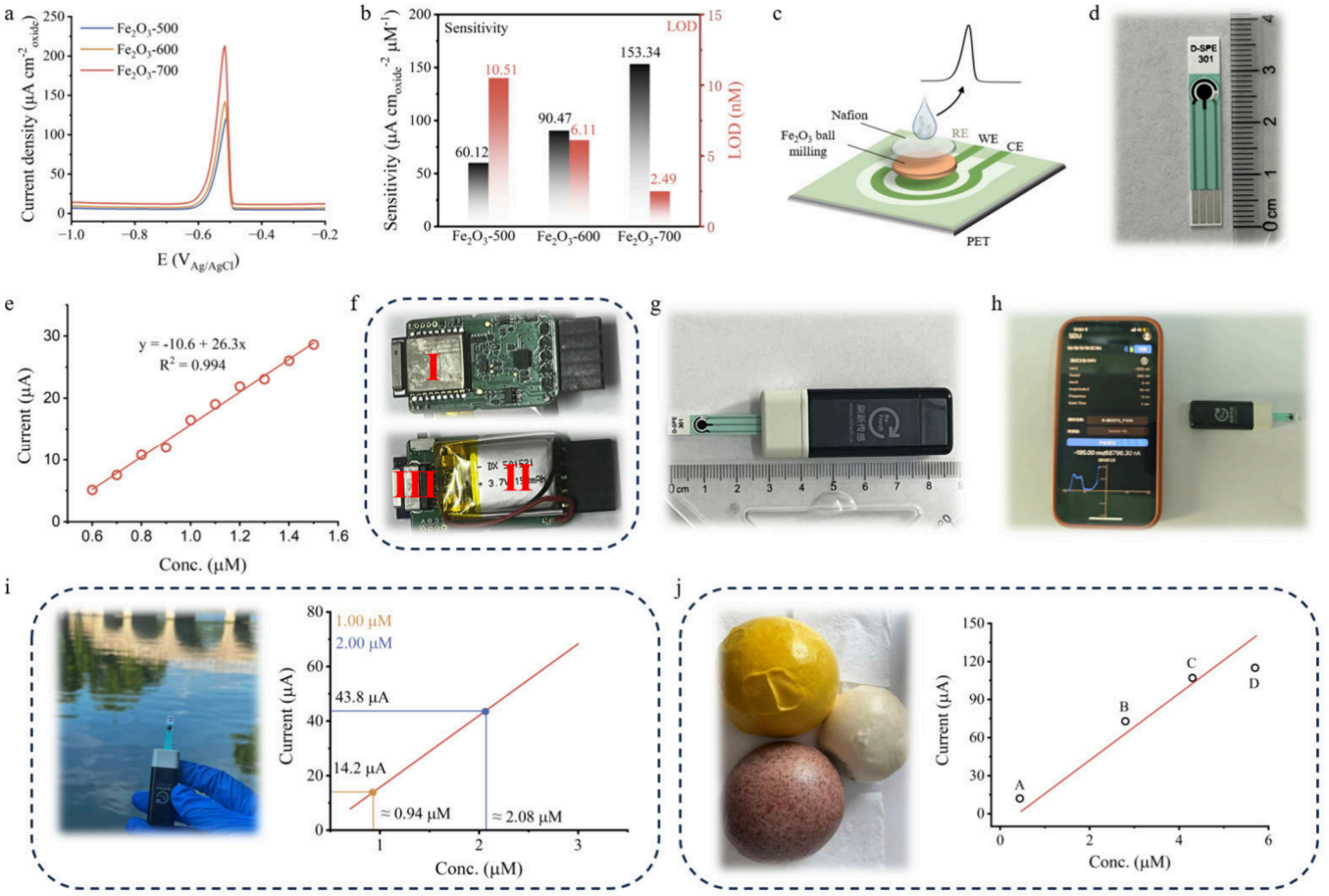

Figure 4. Electrochemical performance and miniaturized electrochemical sensor. (a) SWASV response for 1.6 μM Pb^{2+} detection of α-Fe_2O_3 oxides in 0.1 M NaAc−HAc solution (pH 6.0). (b) Comparisons of detection sensitivities and LODs for Pb^{2+} detection across α-Fe_2O_3 oxides. (c) Scheme for miniaturizing electrochemical sensors. (d) Photograph of the screen-printed electrode. (e) Current density response signals of Fe_2O_3-700 μ_B at different Pb^{2+} concentrations. (f) Front-facing view of the printed circuit board (top). "I" is specifically identified as the Bluetooth module. Rear-facing view of the printed circuit board (bottom). In this depiction, "II" is denoted as the rechargeable battery responsible for powering the sensor, while "III" is highlighted as the charging port. (g) Photograph of the miniaturized electrochemical sensor. (h) Sensor operation interface and sensor photographs. (i) Daming Lake water sampling (left) and comparison of the measured Pb^{2+} concentration with the nominal value in Daming Lake water containing 1 and 2 μM Pb^{2+} (right). (j) Photograph of steamed buns with Pb^{2+}-contaminated water (left) and the signal responses of the microsensor for steamed buns prepared using four types of Pb^{2+}-contaminated water at different concentrations (right).

of α-Fe_2O_3. This shift is attributed to increased electron density around Fe atoms due to the shortening of the Fe−O bond lengths at higher temperatures. X-ray absorption spectroscopy (XAS) measurements were carried out on the α-Fe_2O_3 oxides to analyze the valence state of Fe ions (Figure 2e). The normalized Fe L-edge XAS spectra of Fe_2O_3-500, Fe_2O_3-600, and Fe_2O_3-700 show similar edge positions and spectral features to those of the standard Fe^{3+} reference, indicating that the Fe ions in all three samples predominantly exist in the +3 oxidation state. The oxygen K-edge spectrum shown in Figure 2f and Figure S4 reflects the unoccupied oxygen 2p density of states, originating from the excitation of core O 1s electrons. The leading-edge region (~529.5−534 eV) exhibits multiple local intensity maxima, which are attributed to the hybridization between O 2p orbitals and the 3d orbitals of neighboring transition-metal ions. The trailing-edge region (above ~535 eV) corresponds to the hybridization between O 2p orbitals and the 4s/4p states of adjacent Fe atoms. Among the three α-Fe_2O_3 oxides, Fe_2O_3-700 exhibits the highest overall intensity, suggesting the strongest hybridization between oxygen and Fe atoms, which is consistent with a shorter Fe−O bond length.

To investigate the local Fe−O coordination in α-Fe_2O_3 oxides, Fe K-edge X-ray absorption near-edge structure (XANES) and extended X-ray absorption fine structure (EXAFS) analyses were performed (Figure 3). As shown in Figure 3b, the main peak in the first-shell region is assigned to Fe−O coordination. The EXAFS results indicate a progressive shift of the Fe−O coordination feature to a lower radial distance with increasing calcination temperature, consistent with a shortened Fe−O coordination distance in Fe_2O_3-700 relative to that in Fe_2O_3-600 and Fe_2O_3-500. This trend agrees with the FTIR blue shift and supports the conclusion that increasing calcination temperature leads to shorter Fe−O bonds.

Electrochemical Sensing Performance. Building on the confirmed engineering of Fe−O bond length, the electrochemical sensing performances of α-Fe_2O_3 oxides for HMI detection were investigated by using square wave anodic stripping voltammetry (SWASV). This technology was employed to assess the influence of Fe−O bond length on electrochemical sensing signals. Specifically, 0.1 M HAc-NaAc buffer solution (pH = 6) was employed as the electrolyte, and the deposition process was performed at −1.0 V for 150 s.

https://doi.org/10.1021/acs.jpclett.6c00146
J. Phys. Chem. Lett. 2026, 17, 5037−5044

Table 1. Different Pb^{2+} Concentrations Added to Daming Lake Water and Their Corresponding Current Signals and Calculated Output Concentrations in the Fe_2O_3-700 BM Microelectrochemical Sensor

Sample concentration (μM)	Detection current (μA)	Output concentration (μM)	Recovery Rate (%)	RSD (%)	Concentration in solution (ICP-MS) (μM)
1.00	14.2	0.940	94	3.18	1.00
2.00	43.8	2.08	104	2.65	2.00

Table 2. Corresponding Pb^{2+} Content (ICP-MS) of Steamed Buns Prepared with Four Different Concentrations of Pb^{2+}-Contaminated Water and the Corresponding Current in the Fe_2O_3-700 BM Microelectrochemical Sensor after 1000-Fold Dilution and the Output Concentration and the Calculated Pb^{2+} Content in the Steamed Buns (Electrochemical Sensor)

Number	Polluted water concentration (mM)	Concentration in steamed buns (μM g^{-1}) (ICP-MS)	Detection current (diluted 1000 times) (μA)	Output concentration (μM)	Concentration in steamed buns (μM g^{-1}) (electrochemical sensing)
A	5	0.879	12.1	0.863	1.72
B	10	5.61	72.8	3.17	6.34
C	15	8.59	107	4.47	8.94
D	20	11.4	115	4.78	9.56

Electrochemical sensing of metal ions is fundamentally a surface-driven process, wherein the adsorption and desorption of metal ions take place exclusively on the catalyst surface. Precise evaluation of catalytic intrinsic activity plays a key role in the rational selection of high-performance electrocatalysts. In this study, the specific surface areas of α-Fe_2O_3 oxides were determined using N_2 physisorption based on the BET (Figure S3). Figure 4a displays the current signal responses of the α-Fe_2O_3 oxides at a Pb^{2+} concentration of 1.6 μM. Among these, Fe_2O_3-700 exhibits the highest current response, followed by Fe_2O_3-600, while Fe_2O_3-500 demonstrates the lowest response. The anodic stripping peaks of the Fe_2O_3 oxides appear at around −0.55 V, and the peak current increases linearly with the Pb^{2+} concentration (Figure S6). According to the linear equations (insets of Figure S6), the detection sensitivities of Fe_2O_3-500, Fe_2O_3-600, and Fe_2O_3-700 toward Pb^{2+} ions are 60.12, 90.47, and 153.34 μA cm_{oxide}^{-2} μM^{-1}, respectively. Their theoretical limits of detection (LODs) were calculated to be 10.51, 6.11, and 2.49 nM, respectively (Figure 4b). By contrast, the bare GCE electrode shows no detectable response to 1 μM Pb^{2+} (Figure S7), confirming that the observed activity originates from the Fe_2O_3 materials. We establish a correlation between the Fe−O bond length and the detection performance, observing that a decrease in bond length corresponds to an enhancement in performance (Figure S8).

Miniaturized Electrochemical Sensor. Based on the above conclusion, we developed a miniaturized Pb^{2+} sensor using screen-printed electrodes, which demonstrated excellent performance. In order to expose more active sites, we used ball milling to increase the specific surface area of Fe_2O_3-700. A comparison of the X-ray diffraction and Raman spectroscopy data before and after ball milling reveals that the diffraction peaks of the milled sample are completely consistent with those of the pristine material, with no additional phases detected (Figure S9a). Furthermore, the positions and shapes of the Raman characteristic peaks remain identical, showing no shifts or new vibrational modes (Figure S9b). These results demonstrate that the ball milling process did not alter the crystal structure or chemical bonding environment of the material, indicating that no detectable lattice defects or significant changes in crystallinity were introduced. Next, we evaluated the electrochemical detection performance of Fe_2O_3-700 ball milling (Fe_2O_3-700 μ_B) by using a screen-printed electrode (Figure 4c,d). As shown in Figure 4e and Figure S10, the SWASV response signal increases with the concentration of Pb^{2+}, which can be expressed as a linear relationship. The Fe_2O_3-700 μ_B exhibits a detection sensitivity of 26.3 μA μM^{-1} with a low detection limit of 1.14 nM, significantly outperforming other sensitive interface materials reported in the literature (Table S2). Then the Fe_2O_3-700 μ_B sensor was upgraded to a miniaturized electrochemical tester (Figure 4f,g and Figure S11) for further testing with real water, the environment, and food. The data transmitted wirelessly to the computer and the related statistics are shown in Figure 4g,h. The SWASV data of the Fe_2O_3-700 μ_B electrode obtained in the Daming Lake water containing 1 and 2 μM Pb^{2+} are presented in Figure S12. We found that the measured values were about 0.94 and 2.08 μM, which were close to the actual Pb^{2+} concentrations of 1 and 2 μM (Figure 4i and Table 1).

In response to the Pb^{2+} poisoning incident associated with steamed bread in Tianshui City, Gansu Province, China, we applied the Fe_2O_3-700 μ_B microelectrochemical sensor for food safety monitoring. Conventional methods for detecting heavy metal ions in food, including inductively coupled plasma mass spectrometry, atomic absorption spectrometry, atomic fluorescence spectrometry, and electrochemical methods, share a common limitation: the cumbersome and time-consuming sample pretreatment. Specifically, these procedures often require lengthy digestion or extraction steps, rendering them unsuitable for rapid on-site screening. Consequently, when dealing with complex food matrices, the accuracy of the detection results is frequently compromised by cross-contamination or analyte loss during the pretreatment process. These considerations highlight the need for portable electrochemical platforms that can simplify the analytical workflow and enable the rapid screening of food samples. Steamed bread samples were prepared using four different Pb^{2+}-contaminated water sources (denoted as A, B, C, and D). The preparation of steamed bread and the extraction of Pb^{2+} are detailed in the Methods section. The electrochemical sensor's output signals for Pb^{2+} concentration were compared with inductively coupled plasma mass spectrometry (ICP-MS) measurements. The measurement results of the two methods were similar (Figure 4j, Figure S13, and Table 2). Furthermore, the two data sets are strongly correlated (Figure S14). Therefore, the miniaturized electrochemical tester has an excellent Pb^{2+} detection performance in real water and food samples.

https://doi.org/10.1021/acs.jpclett.6c00146
J. Phys. Chem. Lett. 2026, 17, 5037−5044

In summary, we synthesized α-Fe_2O_3 with varying Fe−O bond lengths and established a correlation among Fe−O bond length, adsorption energy, and electrochemical sensing performance through both computational and experimental approaches. Our findings show that Fe_2O_3-700, with the shortest Fe−O bond length, exhibits the highest electrochemical activity. Accordingly, Fe−O covalency is proposed as a new activity descriptor for the electrochemical detection of HMIs. Furthermore, by ball milling Fe_2O_3-700 to increase its surface area, we fabricated a microelectrochemical sensor for Pb^{2+} detection, achieving a high sensitivity of 26.3 $\mu A \cdot \mu M^{-1}$ and a detection limit of as low as 1.14 nM. The resulting sensor was further validated in real water and food samples, highlighting its potential for on-site heavy-metal analysis. By elucidating the role of the Fe−O bond length in determining sensing performance, this study offers new insights into the rational design of iron-based oxides for next-generation electrochemical sensors.

METHODS

Chemicals. Ferric nitrate nonahydrate [$Fe(NO_3)_3 \cdot 9H_2O$], citric acid, ammonia ($NH_3 \cdot H_2O$), acetic acid (HAc), and sodium acetate (NaAc) were purchased from Shanghai McLean Biochemical Technology Co., Ltd. Lead nitrate was purchased from Sinopharm Chemical Reagent Co., Ltd. Acetate buffer solutions were prepared by mixing HAc and NaAc solutions. All chemicals were of analytical grade and used as received. Deionized water was used throughout for preparing the aqueous solution.

Apparatus. Electrochemical experiments were carried out using a CHI 760E potentiostat (ChenHua Instruments Co., China) with a standard three-electrode system including a glassy carbon electrode (GCE, diameter of 3 mm) as the working electrode, a platinum wire as the counter electrode, and a saturated Ag/AgCl electrode as the reference electrode. XRD was carried out on a Siemens D5000 X-ray diffractometer with Cu Kα radiation (λ = 1.5406 Å). FT-IR was recorded using a Thermo Nicolet 8700 spectrometer. Transmission electron microscopy (TEM) analysis was performed on a Tecnai G2 20 (FEI) instrument at an accelerating voltage of 200 kV. XPS was conducted with monochromatic Al Kα radiation (Thermo Fisher Scientific Co., USA). X-ray absorption spectra (XAS) characterizations were carried out on the beamlines (XMCD) in the Hefei National Synchrotron Radiation Laboratory (NSRL).

Synthesis of α-Fe_2O_3. α-Fe_2O_3 was synthesized using the sol−gel method. A solution of 2 mmol of citric acid and 2 mmol of $Fe(NO_3)_3 \cdot 9H_2O$ was prepared in 5 mL of deionized water. The pH of the solution was adjusted to 10 by the slow addition of ammonia under constant stirring. The solution was then heated to 80 °C and stirred continuously for 2 h to complete the sol−gel process. The resulting gel was dried overnight at 60 °C, ground into powder, and divided into three portions. Each portion was calcined separately at 500, 600, and 700 °C for 6 h at a ramp rate of 10 °C min^{-1} under air flow. The final products were designated as Fe_2O_3-500, Fe_2O_3-600, and Fe_2O_3-700, respectively.

Preparation of Pb^{2+}-Contaminated Steamed Buns and Extraction of Adsorbed Pb^{2+} Ions. Steamed buns were placed in solutions containing varying concentrations of Pb^{2+} ions and heated for 30 min to obtain Pb^{2+}-contaminated steamed buns. A 0.5 g sample of contaminated steamed bun skin was added to 5 mL of 2 M HNO_3 and allowed to soak for 15 min to extract the adsorbed Pb^{2+} ions.

Electrochemical Measurements. To prepare the electrode modification ink, 0.5 mg of α-Fe_2O_3 was dispersed in 1 mL of a solution (deionized water: isopropanol = 1:1). The mixture was sonicated for 30 min to form a homogeneous ink. Prior to modification, the GCE was polished sequentially with 1.0 and 0.3 μm alumina to achieve a clean and smooth surface. Afterward, 4 μL of the prepared ink was carefully dropped onto the surface of the polished GCE. The modified electrode was then left to dry at room temperature, completing the preparation process. The electrochemical behavior of Pb^{2+} was measured by SWASV, which mainly included two working processes. The reduction process of HMIs was performed at −1.0 V vs Ag/AgCl (saturated) for 150 s in 0.1 M HAc-NaAc (pH 6.0). For the desorption process, where the anodic stripping of the electrodeposited HMIs was performed, the electrochemical parameters were as follows: frequency of 15 Hz, amplitude of 25 mV, increment potential of 4 mV, and desorption potential of −1 to −0.2 V for Pb^{2+}. After each test, the modified GCE was regenerated at −1 V for 100 s. The theoretical limit of detection (LOD) is calculated from 3SD/S (3σ method), where SD is the standard deviation of several sets of test data and S is the detection sensitivity.

Computational Details. The α-Fe_2O_3 (001) plane was chosen to conduct the following research because it is the most stable plane for α-Fe_2O_3. The bulk and slab (001) models of α-Fe_2O_3 were constructed with the lattice parameters a = b = 5.03 Å and c = 13.72 Å, respectively. The bulk model consisted of 18 O atoms and 12 Fe atoms, and the surface model was cut from a 2 × 2 × 1 supercell. The final surface model consisted of nine layers with 36 O atoms and 24 Fe atoms, respectively. The atoms of the lower three layers were fixed, and the atoms of the remaining six layers were fully relaxed. The DFT calculation was carried out with the Vienna ab initio simulation package (VASP).[27,28] The exchange-correlation functional was treated within the generalized gradient approximation (GGA)[29] using the Perdew−Burke−Ernzerhof (PBE) formulation. The electron−ion interaction was described by the projector-augmented-wave (PAW) method, with the valence electron configrations of$2s^2 2p^4$ for O, $3d^6 4s^2$ for Fe, and $5d^{10} 6s^2 6p^2$ for Pb, respectively. The DFT+U method was used to describe the strong correlation of d electrons in transition metals, and the U-J value for 3d electrons of Fe atoms was 4 eV.[30] The cutoff energy, the vacuum between slabs, and the K-point sampling were confirmed by convergence tests, which were 650 eV, 20 Å, and 3 × 3 × 2 for the bulk mode and 3 × 3 × 1 for the slab mode. The convergence conditions of energy and force for the self-consistency cycle and ionic relaxation were 10^{-5} eV/atom and −0.02 eV $Å^{-1}$, respectively. The DFT-D3 method[31] was used to describe the van der Waals interaction between HMIs and slabs, and the dipole correction was taken into account for the entire calculation. The adsorption energy could be calculated as $E_{ads} = E_{surface+Pb} - E_{surface} - E_{Pb}$. A more negative E_{ads} indicates stronger adsorption.

ASSOCIATED CONTENT

Data Availability Statement

The data that support the findings of this study are presented in the Letter and Supporting Information and are available from the corresponding authors upon reasonable request.

Supporting Information

The Supporting Information is available free of charge at https://pubs.acs.org/doi/10.1021/acs.jpclett.6c00146.

Most stable magnetic configuration of the α-Fe_2O_3 bulk model (PDF)

N_2 adsorption−desorption isotherms; O K-edge XAS spectra; relationship between Fe−O bond length and sensitivity; and electrochemical detection performance test data (PDF)

Transparent Peer Review report available (PDF)

AUTHOR INFORMATION

Corresponding Authors

Zhaoyong Guan − *School of Chemistry and Chemical Engineering, Shandong University, 250100 Jinan, China;* orcid.org/0000-0002-6847-5809; Email: zyguan@sdu.edu.cn

Bin Cai − *School of Chemistry and Chemical Engineering, Shandong University, 250100 Jinan, China; Shenzhen*

https://doi.org/10.1021/acs.jpclett.6c00146
J. Phys. Chem. Lett. 2026, 17, 5037−5044

Research Institute of Shandong University, Shenzhen 518000, China; orcid.org/0000-0002-3263-0395;
Email: bin.cai@sdu.edu.cn

Authors

Cunyuan Gao − *School of Chemistry and Chemical Engineering, Shandong University, 250100 Jinan, China*
Yutong Wang − *School of Chemistry and Chemical Engineering, Shandong University, 250100 Jinan, China*
Na Zhang − *School of Chemistry and Chemical Engineering, Shandong University, 250100 Jinan, China*
Weiyi Wang − *Hefei National Research Center for Physical Sciences at the Microscale and State Key Laboratory of Precision and Intelligent Chemistry, University of Science and Technology of China, Hefei, Anhui 230026, China;* orcid.org/0000-0001-6981-2611
Qasim Imtiaz − *Department of Chemistry and Chemical Engineering, Lahore University of Management Sciences, 54792 Lahore, Pakistan*

Complete contact information is available at: https://pubs.acs.org/10.1021/acs.jpclett.6c00146

Author Contributions

[⊥]C.G. and Y.W. contributed equally to this work.

Author Contributions

C.G. and Y.W. designed and carried out the experiments. C.G., Y.W., N.Z., W.W., Q.I., and Z.G. wrote the manuscript. B.C. supervised the project. All authors discussed the results and commented on the manuscript.

Notes

The authors declare no competing financial interest.

■ ACKNOWLEDGMENTS

This work was supported by the Natural Science Foundation of Shandong Province (ZR2023YQ039), the Shenzhen Science and Technology Program (JCYJ20250604124247061), the Guangdong Basic and Applied Basic Research Foundation (2026A1515010405), and the Instrument Improvement Funds of Shandong University Public Technology Platform (ts20230110). We are grateful to the National Synchrotron Radiation Laboratory for access to beamline BL12B X-ray magnetic circular dichroism. We thank Shenzhen Refresh Biosensing Technology Co., Ltd. for its help in the construction of the microelectrochemical workstation. The scientific calculations in this letter have been performed on the HPC Cloud Platform of Shandong University, the HPC Platform for Theoretical and Computational Chemistry of the School of Chemistry and Chemical Engineering of Shandong University, the Hefei Advanced Computing Center, and the advanced computing resources provided by the Supercomputing Center of the USTC.

■ REFERENCES

(1) Aragay, G.; Pons, J.; Merkoçi, A. Recent Trends in Macro-, Micro-, and Nanomaterial-Based Tools and Strategies for Heavy-Metal Detection. *Chem. Rev.* **2011**, *111*, 3433−3458.
(2) Bolisetty, S.; Peydayesh, M.; Mezzenga, R. Sustainable technologies for water purification from heavy metals: review and analysis. *Chem. Soc. Rev.* **2019**, *48*, 463−487.
(3) Zhang, Y.; Chen, W.; Dong, X.; Fan, H.; Wang, X.; Bian, L. Simultaneous detection of trace toxic metal ions, Pb^{2+} and Ag^{+}, in water and food using a novel single-labeled fluorescent oligonucleotide probe. *Sensor Actuat. B-Chem.* **2018**, *261*, 58−65.
(4) Mirzaei Karazan, Z.; Roushani, M.; Jafar Hoseini, S. Simultaneous electrochemical sensing of heavy metal ions (Zn^{2+}, Cd^{2+}, Pb^{2+}, and Hg^{2+}) in food samples using a covalent organic framework/carbon black modified glassy carbon electrode. *Food Chem.* **2024**, *442*, 138500.
(5) Li, S.-S.; Li, W.-J.; Jiang, T.-J.; Liu, Z.-G.; Chen, X.; Cong, H.-P.; Liu, J.-H.; Huang, Y.-Y.; Li, L.-N.; Huang, X.-J. Iron Oxide with Different Crystal Phases (α- and γ-Fe_2O_3) in Electroanalysis and Ultrasensitive and Selective Detection of Lead(II): An Advancing Approach Using XPS and EXAFS. *Anal. Chem.* **2016**, *88*, 906−914.
(6) Thakur, A.; Mandal, D.; Ghosh, S. Sensitive and Selective Redox, Chromogenic, and "Turn-On" Fluorescent Probe for Pb(II) in Aqueous Environment. *Anal. Chem.* **2013**, *85*, 1665−1674.
(7) Kim, H. N.; Ren, W. X.; Kim, J. S.; Yoon, J. Fluorescent and colorimetric sensors for detection of lead, cadmium, and mercury ions. *Chem. Soc. Rev.* **2012**, *41*, 3210−3244.
(8) Lu, M.; Deng, Y.; Luo, Y.; Lv, J.; Li, T.; Xu, J.; Chen, S.-W.; Wang, J. Graphene Aerogel−Metal−Organic Framework-Based Electrochemical Method for Simultaneous Detection of Multiple Heavy-Metal Ions. *Anal. Chem.* **2019**, *91*, 888−895.
(9) Chen, S.-H.; Song, Z.-Y.; Xiao, X.-Y.; Huang, H.-Q.; Yang, Y.-F.; Li, P.-H.; Yang, M.; Huang, X.-J. Engineering Electron-Rich Sites on $CoSe_{2-x}$ Nanosheets for the Enhanced Electroanalysis of As(III): A Study on the Electronic Structure via X-ray Absorption Fine Structure Spectroscopy and Density Functional Theory Calculation. *Anal. Chem.* **2022**, *94*, 3211−3218.
(10) Dai, X.; Nekrassova, O.; Hyde, M. E.; Compton, R. G. Anodic Stripping Voltammetry of Arsenic(III) Using Gold Nanoparticle-Modified Electrodes. *Anal. Chem.* **2004**, *76*, 5924−5929.
(11) Hocevar, S. B.; Švancara, I.; Ogorevc, B.; Vytřas, K. Antimony Film Electrode for Electrochemical Stripping Analysis. *Anal. Chem.* **2007**, *79*, 8639−8643.
(12) Li, P.-H.; Song, Z.-Y.; Yang, M.; Chen, S.-H.; Xiao, X.-Y.; Duan, W.; Li, L.-N.; Huang, X.-J. Electrons in Oxygen Vacancies and Oxygen Atoms Activated by Ce^{3+}/Ce^{4+} Promote High-Sensitive Electrochemical Detection of Pb(II) over Ce-Doped α-MoO_3 Catalysts. *Anal. Chem.* **2020**, *92*, 16089−16096.
(13) Gao, C.; Zhen, S.; Wang, Y.; Wang, L.; Cao, Y.; Zhan, J.; Zhang, L.; Cai, B. Spin effects in regulating the adsorption characteristics of metal ions. *Chem. Sci.* **2025**, *16*, 2429−2436.
(14) Xiao, X.-Y.; Song, Z.-Y.; Li, P.-H.; Chen, S.-H.; Li, L.-N.; Yang, M.; Lin, C.-H.; Huang, X.-J. Au_{25} Nanoclusters Exhibit Superhigh Catalytic Activity in Electrochemical Detection of As(III). *Anal. Chem.* **2021**, *93*, 14014−14023.
(15) Gao, C.; Lu, Y.; Wang, Y.; Wang, C.; Hübner, R.; Li, Y.; Zhan, J.; Zhao, M.; Cai, B. Tuning Iron−Oxygen Covalency in Perovskite Oxides for Efficient Electrochemical Sensing. *J. Phys. Chem. C* **2022**, *126*, 17618−17626.
(16) Gao, C.; Yu, X.-Y.; Xiong, S.-Q.; Liu, J.-H.; Huang, X.-J. Electrochemical Detection of Arsenic(III) Completely Free from Noble Metal: Fe_3O_4 Microspheres-Room Temperature Ionic Liquid Composite Showing Better Performance than Gold. *Anal. Chem.* **2013**, *85*, 2673−2680.
(17) Jin, Z.; Yang, M.; Chen, S.-H.; Liu, J.-H.; Li, Q.-X.; Huang, X.-J. Tin Oxide Crystals Exposed by Low-Energy {110} Facets for Enhanced Electrochemical Heavy Metal Ions Sensing: X-ray Absorption Fine Structure Experimental Combined with Density-Functional Theory Evidence. *Anal. Chem.* **2017**, *89*, 2613−2621.
(18) Li, S.-S.; Zhou, W.-Y.; Jiang, M.; Guo, Z.; Liu, J.-H.; Zhang, L.; Huang, X.-J. Surface Fe(II)/Fe(III) Cycle Promoted Ultra-Highly Sensitive Electrochemical Sensing of Arsenic(III) with Dumbbell-Like Au/Fe_3O_4 Nanoparticles. *Anal. Chem.* **2018**, *90*, 4569−4577.
(19) Lai, J.; Shafi, K. V. P. M.; Loos, K.; Ulman, A.; Lee, Y.; Vogt, T.; Estournès, C. Doping γ-Fe_2O_3 Nanoparticles with Mn(III) Suppresses the Transition to the α-Fe_2O_3 Structure. *J. Am. Chem. Soc.* **2003**, *125*, 11470−11471.

(20) Tian, C. M.; Li, W. W.; Lin, Y. M.; Yang, Z. Z.; Wang, L.; Du, Y. G.; Xiao, H. Y.; Qiao, L.; Zhang, J. Y.; Chen, L.; et al. Electronic Structure, Optical Properties, and Photoelectrochemical Activity of Sn-Doped Fe_2O_3 Thin Films. *J. Phys. Chem. C* **2020**, *124*, 12548−12558.
(21) Wang, X.; Wang, T.; Si, G.; Li, Y.; Zhang, S.; Deng, X.; Xu, X. Oxygen vacancy defects engineering on Ce-doped α-Fe_2O_3 gas sensor for reducing gases. *Sensor Actuat. B-Chem.* **2020**, *302*, 127165.
(22) Su, Y.; Yu, W.; Liao, L.; Xiong, X.; Chen, H.; Hu, L.; Lei, T.; Zhao, J.; Chen, D.; Mai, W. Unveiling the Synergy of Interfacial Contact and Defects in α-Fe_2O_3 for Enhanced Photo-Electrochemical Water Splitting. *Adv. Funct. Mater.* **2023**, *33*, 2303976.
(23) Han, Y.; Wang, H.; Huang, D.; Wang, P.; Zhang, J.; Ren, X.; Meng, Y.; Lv, B. Crystal facet-dependent reduction behavior of α-Fe_2O_3 in hydrogen atmosphere. *Appl. Surf. Sci.* **2023**, *638*, 158056.
(24) Cava, C. E.; Roman, L. S.; Persson, C. Effects of native defects on the structural and magnetic properties of hematite α-Fe_2O_3. *Phys. Rev. B* **2013**, *88*, 045136.
(25) Kuznetsov, D. A.; Han, B.; Yu, Y.; Rao, R. R.; Hwang, J.; Román-Leshkov, Y.; Shao-Horn, Y. Tuning Redox Transitions via Inductive Effect in Metal Oxides and Complexes, and Implications in Oxygen Electrocatalysis. *Joule* **2018**, *2*, 225−244.
(26) Suresh, R.; Álvarez, Á.; Sandoval, C.; Ramírez, E.; Santander, P.; Mangalaraja, R. V.; Yáñez, J. Fe_2O_3/NiO nanocomposites: synthesis, characterization and roxarsone sensing by Fourier transform infrared photoacoustic spectroscopy. *New J. Chem.* **2023**, *47*, 12806−12815.
(27) Kresse, G.; Furthmüller, J. Efficiency of ab-initio total energy calculations for metals and semiconductors using a plane-wave basis set. *Comput. Mater. Sci.* **1996**, *6*, 15−50.
(28) Kresse, G.; Furthmüller, J. Efficient iterative schemes for ab initio total-energy calculations using a plane-wave basis set. *Phys. Rev. B* **1996**, *54*, 11169−11186.
(29) Perdew, J. P.; Burke, K.; Ernzerhof, M. Generalized Gradient Approximation Made Simple. *Phys. Rev. Lett.* **1996**, *77*, 3865−3868.
(30) Serdtsev, A. V.; Solodovnikov, S. F.; Medvedeva, N. I. Sodium diffusion and redox properties of alluaudite $Na_{2+2x}M_{2-x}(MoO_4)_3$ (M = Fe, Co, Ni) from DFT+U study. *Mater. Today Commun.* **2020**, *22*, 100825.
(31) Grimme, S.; Antony, J.; Ehrlich, S.; Krieg, H. A consistent and accurate ab initio parametrization of density functional dispersion correction (DFT-D) for the 94 elements H-Pu. *J. Chem. Phys.* **2010**, *132*, 154104.

https://doi.org/10.1021/acs.jpclett.6c00146
J. Phys. Chem. Lett. 2026, 17, 5037−5044